

CORE-COLLAPSE SUPERNOVA EQUATIONS OF STATE BASED ON NEUTRON STAR OBSERVATIONS

A. W. STEINER¹, M. HEMPEL², AND T. FISCHER³

¹ Institute for Nuclear Theory, University of Washington, Seattle, WA 98195, USA

² Department of Physics, University of Basel, Klingelbergstrasse 82, 4056 Basel, Switzerland

³ Institute for Theoretical Physics, University of Wrocław, pl. Maxa Borna 9, 50-204, Wrocław, Poland

Received 2012 July 16; accepted 2013 June 24; published 2013 August 9

ABSTRACT

Many of the currently available equations of state for core-collapse supernova simulations give large neutron star radii and do not provide large enough neutron star masses, both of which are inconsistent with some recent neutron star observations. In addition, one of the critical uncertainties in the nucleon–nucleon interaction, the nuclear symmetry energy, is not fully explored by the currently available equations of state. In this article, we construct two new equations of state which match recent neutron star observations and provide more flexibility in studying the dependence on nuclear matter properties. The equations of state are also provided in tabular form, covering a wide range in density, temperature, and asymmetry, suitable for astrophysical simulations. These new equations of state are implemented into our spherically symmetric core-collapse supernova model, which is based on general relativistic radiation hydrodynamics with three-flavor Boltzmann neutrino transport. The results are compared with commonly used equations of state in supernova simulations of 11.2 and 40 M_{\odot} progenitors. We consider only equations of state which are fitted to nuclear binding energies and other experimental and observational constraints. We find that central densities at bounce are weakly correlated with L and that there is a moderate influence of the symmetry energy on the evolution of the electron fraction. The new models also obey the previously observed correlation between the time to black hole formation and the maximum mass of an $s = 4$ neutron star.

Key words: equation of state – dense matter – hydrodynamics – stars: neutron – supernovae: general

Online-only material: color figures

1. INTRODUCTION

Core-collapse supernovae (SNe) are some of the most energetic events in the Universe. They release several times 10^{53} erg in neutrinos, the gravitational binding energy difference between iron core and neutron star, and in case of SN explosions several 10^{51} erg kinetic energy of the ejected material. The latter are related to the standing accretion shock (SAS) revival, which forms when the supersonically collapsing stellar core reaches nuclear matter densities and bounces back. The shock wave initially propagates out of the stellar core and thereby loses energy due to the dissociation of infalling heavy nuclei and electron neutrino escapes when it crosses the neutrinospheres. Several explosion mechanisms have been discussed, i.e., magnetorotational by LeBlanc & Wilson (1970), dissipation of sound waves by Burrows et al. (2006), and the standard scenario driven by neutrino heating by Bethe & Wilson (1985).

The equation of state (EOS) is one of the critical and highly uncertain microphysical inputs for modeling core-collapse SNe. The EOS in SN simulations has to handle several intrinsically different regimes. For temperatures below about 0.5 MeV, time-dependent nuclear reactions are important in determining the nuclear composition. Above 0.5 MeV, nuclear statistical equilibrium (NSE) can be applied, where the dependence of the EOS can be reduced to the three independent variables: temperature T , baryon number density n_B , and proton-to-baryon ratio (or equivalently the electron fraction) Y_e . Finally, at densities close to and above nuclear matter density, the transition to a state of matter composed of deconfined quarks may take place.

While accurate neutron star mass measurements of double pulsar systems are plentiful, reliable radius measurements have

only recently become available. Steiner et al. (2010) obtained quantitative constraints on the EOS of nuclear matter from mass and radius measurements from quiescent low-mass X-ray binaries and objects with photospheric radius expansion bursts. Current neutron star radius observations suggest small radii and lower pressures just above the nuclear saturation density. Small neutron star radii may be interesting for SN dynamics, because they imply more gravitational binding energy. Unfortunately, very few available SN EOS give (1) nuclear matter properties consistent with those inferred from experiment, (2) maximum neutron star masses large enough to be consistent with the recent measurement of a 1.97 M_{\odot} neutron star in Demorest et al. (2010), and (3) masses and radii consistent with recent neutron star observations of, e.g., Steiner et al. (2010). Furthermore, most available EOS tables are based on interactions with larger values of the density derivative of the nuclear symmetry energy, L , even though lower values are suggested by both intermediate-energy heavy-ion collisions (Tsang et al. 2009), chiral effective field theory (Hebeler et al. 2010; Tews et al. 2013), and neutron star radii (Steiner & Gandolfi 2012; Steiner et al. 2013).

We note that there are potential systematic uncertainties in the neutron star mass and radius measurements which are not yet taken into account. The relationship between the Eddington flux and the point at which the photosphere returns to the neutron star surface is not under control (Steiner et al. 2010), the evolution of the spectrum during the tail of the burst is not well understood (Suleimanov et al. 2011), and the value of the factor which corrects for the fact that the X-ray spectrum is not a blackbody may also modify inferred radii. Also, the X-ray spectrum may be modified by accretion and violations of the assumed spherical symmetry. Recent work (Steiner et al. 2013) finds that neutron star radii may be as large as 13 km.

In this article, we construct new EOSs which are both consistent with experimental nuclear data and recent neutron star mass observations. We parameterize nucleonic matter with a new relativistic mean field (RMF) model. In addition to the fitting of the nucleon interactions, we also include nuclei and non-uniform nuclear matter, based on the statistical model from Hempel & Schaffner-Bielich (2010). The final EOS is also provided in tabular form, covering a wide range in density, temperature, and electron fractions. We apply these EOS tables in core-collapse SN simulations of intermediate- and high-mass progenitors. While some recent works have also generated RMF models using similar sets of constraints (Fattoyev et al. 2010; Agrawal et al. 2012), these previous works did not generate full EOS tables for use in core-collapse SN simulations.

2. EQUATIONS OF STATE

The most commonly used EOSs are that of Lattimer & Swesty (1991, hereafter LS), which is based on the compressible liquid-drop model including surface effects, and Shen et al. (1998, hereafter STOS), which is based on the TM1 RMF interaction (Sugahara & Toki 1994) and uses the Thomas–Fermi approximation to describe non-uniform nuclear matter. Both EOSs simplify the baryon composition using the single-nucleus approximation (SNA) for heavy nuclei, and ignore all light nuclei except for alpha particles. There are several studies of the differences between these two EOSs in core-collapse simulations (see, e.g., Sumiyoshi et al. 2006, 2007; Fischer et al. 2009; O’Connor & Ott 2011; Hempel et al. 2012). More recently, several new EOS based on RMF interactions have become available. The new hadronic EOS tables of G. Shen (Shen et al. 2011a, 2011b) are based on NL3 (Lalazissis et al. 1997) and FSUGold (Todd-Rutel & Piekarewicz 2005) RMF interactions with nuclei described in the Hartree approximation. The EOS model of Hempel & Schaffner-Bielich (2010, hereafter HS) and Hempel et al. (2012) is based on the statistical approach and is also used in the present study. It goes beyond SNA by including the detailed nuclear composition, based on experimentally measured nuclear masses as well as different theoretical mass models. Tables are available for eight different RMF parameterizations, including TM1, FSUGold, and TMA (Toki et al. 1995) and the new parameterizations SFHo and SFHx developed in the present article.

There are several critical parameters for characterizing the EOS of hadronic matter, and some of the most relevant and yet uncertain parameters are the nuclear incompressibility, K , the symmetry energy at the saturation density, J , and the logarithmic derivative of the symmetry energy L . The compressibility was an important parameter for early core-collapse simulations (Baron et al. 1985), but only for extreme cases which were not even consistent with the Hulse–Taylor pulsar (Swesty et al. 1994). The compressibilities of the LS EOS tables are available for 180, 220, and 375 MeV. However, the lowest and highest of these values are far outside the currently acceptable range of 240 ± 10 MeV (Colo et al. 2004). We note that there is still some model dependence in extracting this value (Piekarewicz 2010; Khan & Margueron 2012) so that an error bar of 20 MeV is maybe more appropriate, as also reported in Shlomo et al. (2006). Early core-collapse SN simulations also suggested that the symmetry energy is important (Swesty et al. 1994; Sumiyoshi et al. 1995). Recent constraints on J suggest $28 < S < 34$ from a combination of constraints from experiments, theory, and observations of neutron star masses and

radii (Hebeler et al. 2010; Steiner & Gandolfi 2012; Lattimer & Lim 2013; Tsang et al. 2012; Steiner et al. 2013; Tews et al. 2013). While a general trend is slowly emerging, we note that many of these constraints are model-dependent and are not always consistent with each other. Only one of the original SN EOS tables, the LS table with $K = 220$ MeV, obeys the current constraints on these EOS parameters, even though its value of L is larger than would typically be expected for the corresponding J value.

For the new EOSs SFHo and SFHx, we choose to use a covariant Lagrangian based on the Walecka model where nucleons interact via the exchange of σ , ω , and ρ mesons in the mean-field approximation. The non-linear Walecka model is well known to have a limited range of variation in the isospin sector and the nuclear symmetry energy is controlled entirely through the coupling of the nucleons to the ρ meson. In order to provide more flexibility, several additional terms like ρ^4 and $\sigma^2\rho^2$ have been considered. We use the parameterization in Steiner et al. (2005) which provides enough freedom to modify the low- and high-density parts of the isospin sector separately. There are 17 parameters including the scalar–isoscalar meson mass m_σ , the standard non-linear Walecka model couplings g_σ , g_ω , g_ρ , b , and c , the two fourth-order vector meson couplings ζ and ξ , and the parameters a_{1-6} and b_{1-3} which control the symmetry energy as a function of density. These parameters are varied to ensure that both EOSs have saturation properties which agree with that predicted from nuclear masses and giant monopole resonances. In addition, both predict binding energies and charge radii for ^{208}Pb and ^{90}Zr that are within 2% of the experimental values. We ensure that the pressure of neutron matter is always positive and always increases as a function of the density. We ensure that the maximum mass is larger than $1.93 M_\odot$ (the lower 1σ limit from Demorest et al. 2010). We compare our results to LS(180) and FSUGold even though these are inconsistent with this maximum mass because LS(180) is still commonly used in the SN community and to cover also extreme scenarios in our comparison. The requirement that the speed of sound is not superluminal is automatically enforced in this fully covariant model. In our baseline model, SFHo, we also fit the most probable mass–radius curve from Steiner et al. (2010), and in our extreme model, SFHx, we attempt to minimize the radius of low-mass neutron stars yet remaining consistent with the other constraints given above. This forces the value of L for SFHx to be on the lower edge of the typical range of 20–120 MeV. We always take the mass of the neutron to be 939.565346 MeV, the mass of the proton to be 938.272013 MeV, the mass of the ω meson to be 762.5 MeV, the mass of the ρ meson to be 770 MeV, and we use $\hbar c = 197.3269631$ MeV fm (Mohr et al. 2008). The full parameter list for both models is given in Table 1. The saturation properties, nuclear binding energies, and nuclear charge radii for our models are given in Tables 2 and 3. We remark that the values given in Table 2 can be slightly different to previously published ones, e.g., by Hempel et al. (2011), due to a different treatment of the nucleon rest masses. In the present work, we are using the measured masses from above for all of the HS EOS, to obtain the correct low-density limit. This treatment also leads to a slight splitting of the neutron and proton effective masses, m_n^* and m_p^* , respectively. The value of J for LS in Table 2 differs from the published value by Lattimer & Swesty (1991) of 29.3 MeV. These authors computed J as the energy difference between neutron and nuclear matter, whereas we are calculating J as the second derivative with respect to Y_e at the saturation point.

Table 1
RMF Model Parameters

Quantity	Unit	SFHo	SFHx
c_σ	fm	3.1780	3.4016
c_ω	fm	2.2726	2.5730
c_ρ	fm	2.4047	2.4199
b		7.4653×10^{-3}	4.8157×10^{-3}
c		-4.0887×10^{-3}	-4.3984×10^{-3}
ζ		-1.7013×10^{-3}	4.4218×10^{-3}
ξ		3.4525×10^{-3}	2.0535×10^{-4}
a_1	fm ⁻¹	-2.3016×10^{-1}	-4.6241×10^{-1}
a_2		5.7972×10^{-1}	1.6604
a_3	fm	3.4446×10^{-1}	1.1792×10^{-2}
a_4	fm ²	3.4593	2.1595×10^1
a_5	fm ³	1.3473	1.5478
a_6	fm ⁴	6.6061×10^{-1}	8.5506×10^{-1}
b_1		5.8729	8.4606
b_2	fm ²	-1.6442	-2.3629
b_3	fm ⁴	3.1464×10^2	4.0622×10^1
m_σ	fm ⁻¹	2.3714	2.3844

In Table 2, we also give the saturation density n_B^0 , the binding energy of nuclear matter E_0 , the skewness of nuclear matter K' , the reduced neutron and proton effective masses at saturation, the radii of $1.4 M_\odot$ neutron stars at $T = 0$, the maximum mass at $T = 0$, and the maximum mass for stars with constant entropy $s = 4$ in beta equilibrium without neutrinos. The $T = 0$ EOSs for all of the models constructed with nucleon degrees of freedom are given in Figure 1, along with the constraints from Steiner et al. (2010). Figure 2 gives the corresponding mass versus radius curves and also the constraints from Steiner et al. (2010).

For densities below saturation density, we apply the statistical model from HS for the description of non-uniform nuclear matter in NSE, i.e., for the formation of light and heavy nuclei within the gas of unbound nucleons. For the unbound nucleons, we utilize the SFHo and SFHx RMF interactions. At low densities, the description of nuclei is based on measured experimental binding energies (Audi et al. 2003), which are combined with theoretical nuclear structure calculations for exotic nuclei without measured data. Here the finite range droplet model of Möller et al. (1995) was chosen because of its excellent reproduction of experimental binding energies, with a rms deviation of only 0.669 MeV. Due to the use of nuclear structure data, shell effects are automatically included. HS goes beyond the SNA and utilizes a distribution of different nuclear species, and the results for light nuclei are in agreement with more sophisticated quantum many-body models (Hempel

Table 3
Properties of Nuclei for SFHo and SFHx

	$E(^{208}\text{Pb})$ (MeV)	$R(^{208}\text{Pb})$ (fm)	$E(^{90}\text{Zr})$ (MeV)	$R(^{90}\text{Zr})$ (fm)
SFHo	-7.76	5.44	-8.60	4.19
SFHx	-7.87	5.41	-8.55	4.19

et al. 2011). Also, the recent experimental study of Qin et al. (2012) indicates that the HS model is well suited for the description of matter at finite temperature and densities around a few tenths of saturation density. At even larger densities in the HS model, the disappearance of nuclei and smooth transition to uniform nuclear matter is assured by an excluded volume description. Finally we calculate the EOS in tabular form, covering densities from 10^{-12} to 10 fm^{-3} , temperatures from 0.1 to 160 MeV, and electron fractions from 0 to 0.6, including detailed information about the nuclear composition and the thermodynamic properties. The tables are suitable for use in astrophysical simulations and are available online.⁴ The resulting EOS will be compared below with the LS EOS, with the different compressibilities 180 MeV (LS(180)), and 220 MeV (LS(220)), and with STOS.

3. CORE-COLLAPSE SUPERNOVA SIMULATIONS

In this section, we will compare results from SN simulations obtained using the SFHo and SFHx EOSs with the standard EOS LS(220) and the two TM1 RMF parameterizations STOS and HS.

3.1. Supernova Model

Our core-collapse SN model, AGILE-BOLTZTRAN, is based on general relativistic radiation hydrodynamics in spherical symmetry. It employs three-flavor Boltzmann neutrino transport (see Liebendoerfer et al. 2004 and references therein). Table 4 lists the weak processes considered. For the charged-current reactions with nucleons, we apply Reddy et al. (1998) in the zero-momentum transfer approximation (Bruenn 1985). For these rates, we include the nucleon potentials computed for each EOS explicitly, which modify the vacuum Q value due to medium modifications at the mean-field level. These medium modifications of the reaction rates have been shown recently in Martínez-Pinedo et al. (2012) to affect the later evolution of the neutrino spectra after the SN explosion has been launched (see also Roberts et al. 2012a). However, they leave no imprint on the

⁴ See <http://phys-merger.physik.unibas.ch/~hempel/eos.html>.

Table 2
Properties at Saturation Density and Neutron Star Properties for the Different EOSs Under Investigation

EOS	n_B^0 (fm ⁻³)	E_0 (MeV)	K (MeV)	K' (MeV)	J (MeV)	L (MeV)	m_n^*/m_n -	m_p^*/m_p -	$R_{1.4}$ (km)	$M_{T=0,\text{Max}}$ (M_\odot)	$M_{S=4,\text{Max}}$ (M_\odot)
SFHo	0.1583	16.19	245.4	-467.8	31.57	47.10	0.7609	0.7606	11.88	2.059	2.27
SFHx	0.1602	16.16	238.8	-457.2	28.67	23.18	0.7179	0.7174	11.97	2.130	2.36
STOS(TM1)	0.1452	16.26	281.2	-285.3	36.89	110.79	0.6344	0.6344	14.56	2.23	2.62
HS(TM1)	0.1455	16.31	281.6	-286.5	36.95	110.99	0.6343	0.6338	13.84	2.21	2.59
HS(TMA)	0.1472	16.03	318.2	-572.2	30.66	90.14	0.6352	0.6347	14.44	2.02	2.48
HS(FSUgold)	0.1482	16.27	229.5	-523.9	32.56	60.43	0.6107	0.6102	12.52	1.74	2.34
LS(180)	0.1550	16.00	180.0	-450.7	28.61	73.82	1	1	12.16	1.84	2.02
LS(220)	0.1550	16.00	220.0	-411.2	28.61	73.82	1	1	12.62	2.06	2.14

Note. The definition of all the quantities is given in the text.

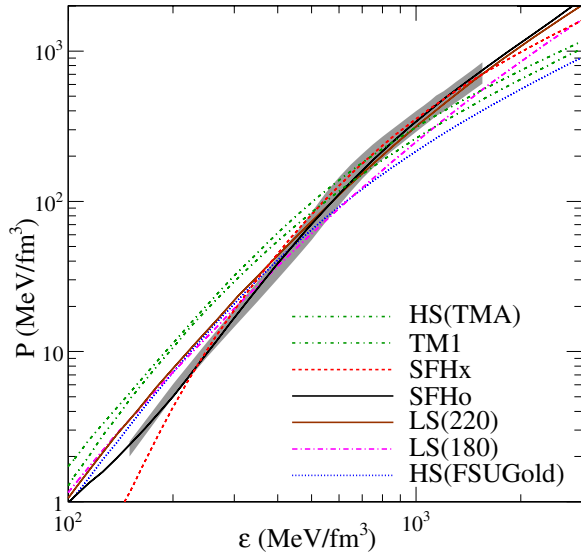


Figure 1. Pressure of zero temperature beta-equilibrium matter as a function of the total energy density. The gray region gives the 1σ confidence limits on the EOS from Steiner et al. (2010). The curve labeled TM1 applies for both the HS(TM1) and STOS EOSs.

(A color version of this figure is available in the online journal.)

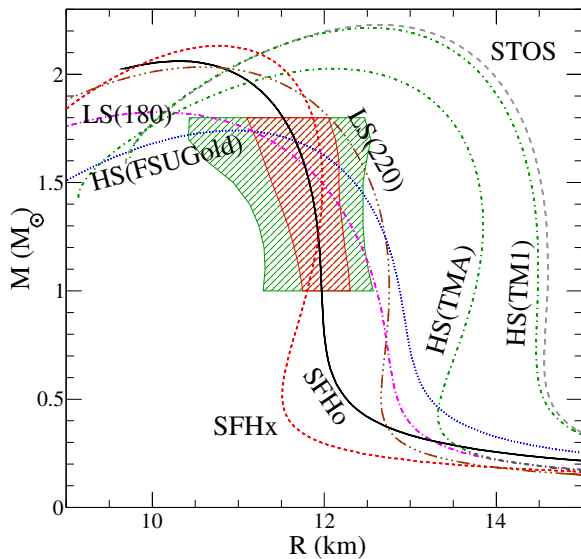


Figure 2. Neutron star mass–radius curve for modern supernova equations of state. The red (green) region outlines the 1σ (2σ) confidence limits from Steiner et al. (2010).

(A color version of this figure is available in the online journal.)

accretion phase prior to the onset of explosion, which is subject of the present paper. For the nucleon charged-current rates we also take into account corrections due to the presence of nuclei (M. Hempel et al. 2013, in preparation). For electron captures on heavy nuclei we include the improved rates from Juodagalvis et al. (2010). Moreover, nucleon recoil is included based on Horowitz (2002) for scattering on nucleons, and the annihilation of trapped electron neutrino pairs has been implemented in Fischer et al. (2009) following Buras et al. (2003).

For NSE conditions ($T > 0.45$ MeV), we implement the baryon EOS tables specified above. For non-NSE, we assume the ideal gas EOS for which we compute abundance changes and energy generation from nuclear burning using a small (20 nuclear species) α -network, based on the nuclear composi-

Table 4
Neutrino Reactions Considered Including References

Reaction ^a	References
$\nu_e + n \rightleftharpoons p + e^-$	Reddy et al. (1998)
$\bar{\nu}_e + p \rightleftharpoons n + e^+$	Reddy et al. (1998)
$\nu_e + (A, Z - 1) \rightleftharpoons (A, Z) + e^-$	Juodagalvis et al. (2010)
$\nu + N \rightleftharpoons \nu' + N$	Bruenn (1985)
$\nu + (A, Z) \rightleftharpoons \nu' + (A, Z)$	Mezzacappa & Bruenn (1993a), Bruenn (1985)
$\nu + e^\pm \rightleftharpoons \nu' + e^\pm$	Mezzacappa & Bruenn (1993a), Bruenn (1985), Mezzacappa & Bruenn (1993b)
$\nu + \bar{\nu} \rightleftharpoons e^- + e^+$	Bruenn (1985)
$\nu + \bar{\nu} + N + N \rightleftharpoons N + N$	Mezzacappa & Messer (1999)
$\nu_e + \bar{\nu}_e \rightleftharpoons \nu_{\mu/\tau} + \bar{\nu}_{\mu/\tau}$	Hannestad & Raffelt (1998) Buras et al. (2003)

Note. ^a $\nu = \{\nu_e, \bar{\nu}_e, \nu_{\mu/\tau}, \bar{\nu}_{\mu/\tau}\}$ and $N = \{n, p\}$.

tion given by the progenitor model. It allows, e.g., for a smooth NSE-to-non-NSE transition as well as to simulate a large domain of the progenitor star (for details, see Fischer et al. 2010). On top of the baryons, also for NSE, contributions from electrons, positrons, and photons are added to the EOS using Timmes & Arnett (1999).

The simulations we will discuss below are launched from iron-core progenitors. We use the $11.2 M_\odot$ model from Woosley et al. (2002) for regular core-collapse SNe and the $40 M_\odot$ from Woosley & Weaver (1995) for the black hole formation scenario. None of the spherically symmetric simulations results in an explosion for the considered simulation times.

3.2. Simulation Results

A detailed SN EOS comparison study for LS(180), LS(220), and STOS, as well as several HS EOS tables with different RMF parameterizations, has been published very recently in Hempel et al. (2012). Here, we extend their analysis and include in addition SFHo/SFHx.

During the contraction of the stellar core, the baryon composition is dominated by heavy nuclei. At low temperatures in non-NSE, the ideal-gas EOS has been applied in all simulations. Abundance changes and the resulting energy generation are taken into account using our simplified nuclear reaction network. Hence, all SN simulations lead to very similar structures at low temperatures, see, e.g., the equal entropy per baryon profiles in the outer layers ($M_B > 1.3 M_\odot$) as illustrated in Figure 3. The exception is LS(220), which is based on a different transition from NSE to non-NSE using a the nuclear mixture of Fe, Ni, and Si (see the entropy per baryon drop between 1.1 and $1.3 M_\odot$ in Figure 3). Structural differences arise at higher temperatures in NSE, which will be discussed below. In general, low-density differences (i.e., the layer above the bounce shock between $0.6 < M_B < 1.3 M_\odot$ in Figure 3) between STOS and HS(TM1) are related to the different description of heavy nuclei. The statistical approach of HS is largely based on experimentally known masses including shell effects. It resembles the ideal gas of $^{56}\text{Ni}/^{56}\text{Fe}$ at the transition to non-NSE by construction. In contrast, the Thomas–Fermi approximation of STOS gives heavy nuclei which are too strongly bound and does not perform well at this transition. Hempel et al. (2012) explained how these differences affect the Y_e evolution. Furthermore, entropy differences between STOS and HS(TM1) originate from the missing kinetic entropy contribution of heavy nuclei in STOS.

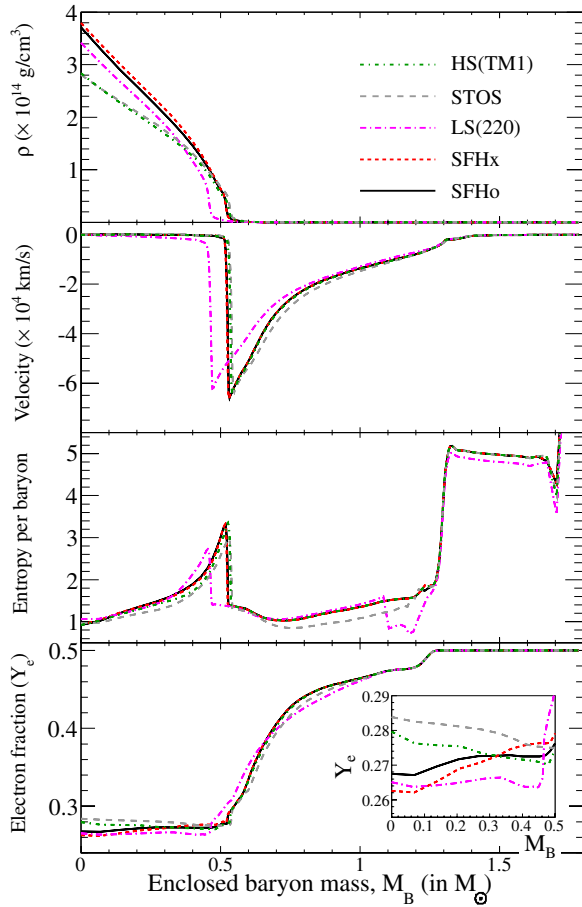


Figure 3. Bounce profiles of selected quantities for the $11.2 M_{\odot}$ models, comparing the different EOS under investigation.

(A color version of this figure is available in the online journal.)

Since we use the same low-density description for nuclei as in **HS**, simulations using **SFHo** and **SFHx** result in the same conditions during the core-collapse phase.

Only a few tens of milliseconds before core bounce, nuclear saturation density is reached at the center. At these conditions high-density EOS differences become large which in turn lead to different dynamical evolutions. We define the moment of core bounce when the central density reaches its maximum before shock breakout. The two TM1 EOSs, **STOS** and **HS(TM1)**, result in the lowest central densities. Differences between **STOS** and **HS(TM1)** are due to the different descriptions of heavy nuclei, as already discussed above. Furthermore, the presence of light nuclei below nuclear saturation density, which are also taken into account in **HS** explicitly, has an impact on thermodynamic properties (for details, see Hempel et al. 2012). **SFHo** and **SFHx** reach similarly high central densities and low central Y_e at core bounce (see Figure 3). Comparing the different EOS in more detail, we find that the central densities appear correlated with the slope of the symmetry energy. A higher L value leads to higher pressures around saturation density and above, and therefore to lower densities at bounce. Note, however, that the maximum central density reached at bounce is also influenced by K , which can weaken this correlation. This does not seem to be a problem here, because the incompressibilities of **LS(220)**, **SFHx**, and **SFHo** are in a similar range, and the high value of K of **STOS** and **HS(TM1)** decrease the central densities even further.

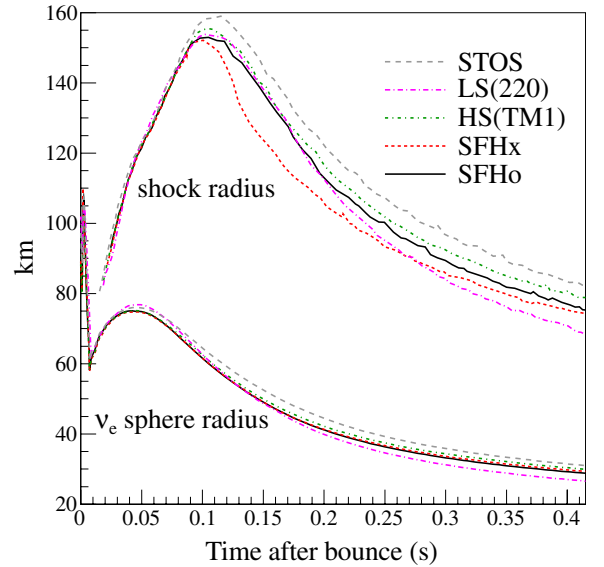


Figure 4. Evolution of the shock radii (thick lines) and ν_e spheres (thin lines) for the $11.2 M_{\odot}$ models, comparing the different EOS under investigation. (A color version of this figure is available in the online journal.)

For the Y_e profiles the situation is more complicated. Our new models, **SFHo** and **SFHx**, tend to give low electron fractions for $M_B < 0.3 M_{\odot}$, but **LS(220)** typically has the lowest electron fraction. Comparing **HS(TM1)** with **STOS** there are pronounced differences, despite practically identical nuclear matter properties. These differences are only caused by the different description of nuclei used in the two EOSs. If we only compare the EOSs which treat nuclei in the same way, namely **HS(TM1)**, **SFHx**, and **SFHo**, then it is possible to identify the effect of the symmetry energy. Around saturation density, i.e., at masses around $0.2 M_{\odot}$, the values of Y_e of these three models increase with J . The behavior of Y_e in the center, at the highest densities, is more connected with L . Models **SFHx** and **LS(220)** have similar values of J , and the lower value in L in **SFHx** implies a smaller symmetry energy at the higher densities encountered in the center. This leads to a lower central Y_e for **SFHx**.

The central object formed at core bounce, i.e., the protoneutron star (PNS), is hot and lepton rich in which sense it differs from the final remnant neutron star. After bounce, the shock starts to propagate outward with initially positive velocities. Simultaneously, mass accretion from the outer part of the stellar core continuously grows the mass of the PNS. Moreover, the expanding bounce shock loses energy due to heavy-nuclei dissociation and neutrino emission. The neutrino emission is related to a large number of electron captures on protons during the shock passage across the neutrinospheres. It releases a burst of ν_e of several 10^{53} erg s^{-1} for a short timescale between 5 and 20 ms after core bounce. Both sources of energy loss turn the expanding and dynamic (i.e., accompanied with matter outflow) bounce shock into an accretion front, the SAS, already between 5 and 10 ms after core bounce. The later PNS evolution is determined from mass accretion and the subsequent PNS compression which leads to continuously rising central density and temperature. For a given mass accretion rate, determined from the progenitor, and otherwise identical simulation setup, the timescale for the PNS compression is directly related to the EOS. On timescales on the order of several 100 ms, EOS differences lead to different neutrinospheres and shock radii, displayed in Figure 4. The neutrinospheres can be used to characterize the size of the central PNS as they are located in its

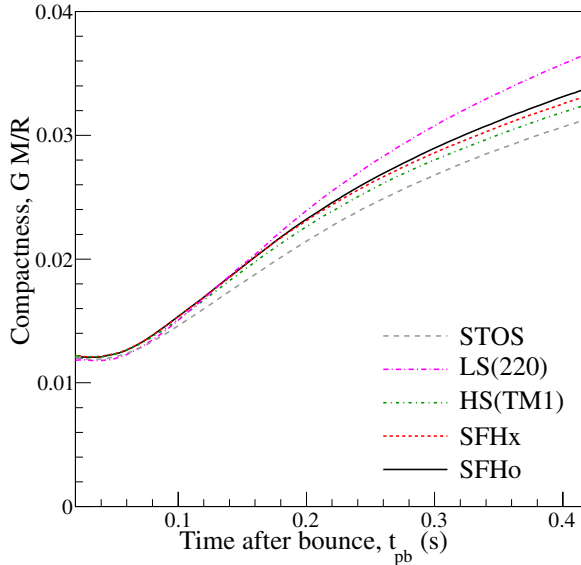


Figure 5. The compactness of the protoneutron star after bounce, defined by the gravitational enclosed mass and radius of the electron neutrinosphere. (A color version of this figure is available in the online journal.)

outer envelope. A general trend can be recognized, EOSs with lower values of L lead to smaller shock radii. The exception is the shock evolution of **LS(220)** which tends to fall back faster than the other models. By comparing **HS(TM1)** with **STOS**, one can identify the effect of the different treatment of heavy nuclei and in addition the inclusion of light nuclei for **HS** and also for **SFHo/SFHx** (for details, see Hempel et al. 2012).

It is difficult to predict astrophysical simulation results from only nuclear matter properties at saturation density (ρ_0) and zero temperature. For example, both **HS(TM1)** and **STOS** are based on the same nucleon interactions TM1 (see Table 3). However, the additional inclusion of light nuclei and the different description of heavy nuclei, relevant for sub-saturation densities, has a significant impact on the conditions at bounce and then also on the later PNS structure and contraction behavior. The early PNS evolution for our new parameterizations **SFHo** and **SFHx**, up to about 100 ms post-bounce, resembles those of **HS(TM1)** (see the neutrinospheres in Figure 4). After this time, the PNS contraction proceeds more quickly in **SFHo/SFHx** than in **HS(TM1)**, reflecting the softer high-density EOS. On timescales of several 100 ms, the PNS and shock contractions slow down for all the RMF EOSs as a consequence of the continuously growing enclosed mass. This effect is significantly weaker for the non-relativistic **LS(220)** EOS.

Figure 5 shows the evolution of the compactness, GM/R . We evaluate these quantities at the electron neutrinosphere, representative of the PNS surface. **SFHo** and **SFHx** result in the most compact PNSs at core bounce, but 100 ms after bounce **LS(220)** becomes more compact.

Figure 6 shows the post-bounce evolution of the neutrino luminosities and their average energies comparing all EOS under investigation. They are sampled in the comoving frame of reference at a distance of 1000 km. Before bounce, only electron neutrinos are produced from electron captures on mainly heavy nuclei. During core contraction, these electron captures lead to a slow rise of the luminosity from 10^{50} to 10^{53} erg s $^{-1}$ on timescales of the order of a few hundred ms. The average ν_e energies rise accordingly from 5 to 10 MeV. The reaction rate for electron captures on nuclei depends on

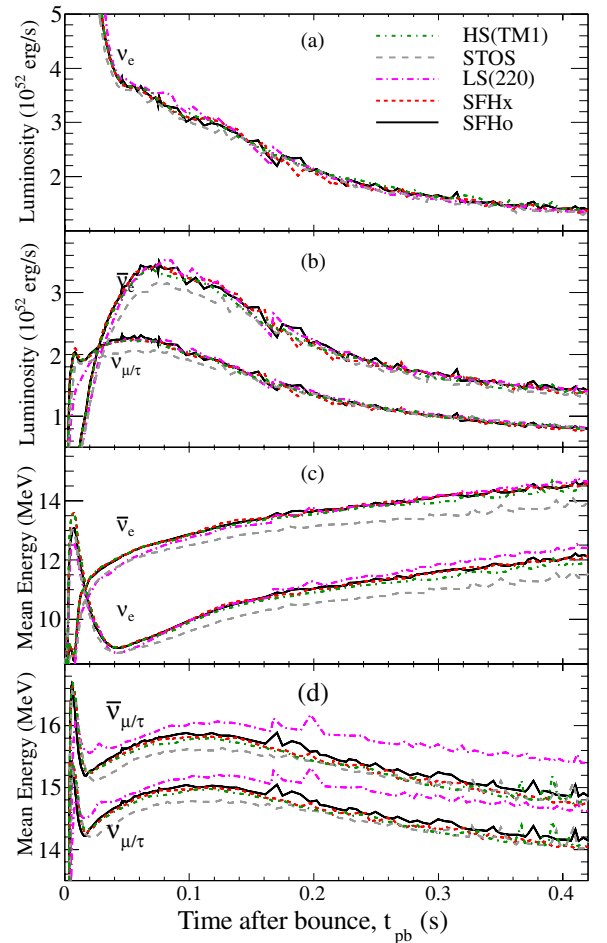


Figure 6. Neutrino luminosities and average energies for all flavors. (A color version of this figure is available in the online journal.)

the density of nuclei. At conditions during the core-collapse phase, i.e., low densities (10^{10} – 10^{12} g cm $^{-3}$) and temperatures ($T = 0.5$ – 2 MeV), the nuclear composition of all EOS under investigation are quantitatively very similar, and so are the resulting neutrino luminosity and average energy evolutions. For a detailed discussion of the collapse phase, see Hempel et al. (2012). Slightly before bounce, when normal nuclear matter density is reached and nuclei dissociate into homogeneous nuclear matter composed of free neutrons and protons, high-density EOS differences lead to qualitatively different neutrino luminosity and average energy evolutions, e.g., the magnitude of the deleptonization burst. However, of relevance here is the post-bounce evolution after the deleptonization burst has been launched ~ 20 ms post-bounce. There is a timescale of several 100 ms during which the SN explosion is expected to be launched, i.e., the shock revival, e.g., via neutrino heating. The evolution of the ν_e luminosities, illustrated in Figure 6(a), differ only marginally for the EOS under investigation because they decouple at low densities where all EOS under investigation are similar. The average energies, on the other hand, are an indicator for the thermalization that neutrinos experience before decoupling from matter that is related to the thick and growing layer of material accumulated onto the PNS surface during the mass-accretion phase prior to shock revival. Since ν_e decouple at lowest densities, their average energies can be used to probe the compactness of layer of accumulated material above the PNS surface. **STOS** and **HS(TM1)** result in the least

Table 5

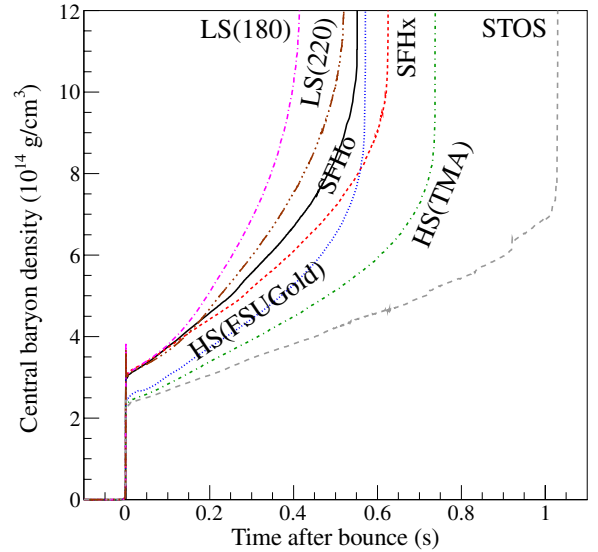
Selected Quantities at the Onset of PNS Collapse and Black Hole Formation

EOS	t_{pb}^{a} (s)	ρ^{b} ($10^{15} \text{ g cm}^{-3}$)	T^{c} (MeV)	M_{B}^{d} (M_{\odot})	M_{G}^{e} (M_{\odot})
LS(180)	0.415	1.292	29.978	2.227	2.133
LS(220)	0.521	1.324	31.446	2.350	2.233
SFHo	0.551	1.067	46.691	2.477	2.347
HS(FSU _{gold})	0.571	1.058	48.104	2.465	2.341
SFHx	0.625	0.803	40.830	2.552	2.424
HS(TMA)	0.737	0.943	46.708	2.626	2.466
STOS	1.028	0.769	49.705	2.864	2.652

Notes.^a Time post-bounce.^b Central baryon density.^c Central temperature.^d Enclosed baryon mass.^e Enclosed gravitational mass.

compact configurations with the thickest layer of accumulated material and hence the ν_e experience most thermalization before decoupling, and hence the average energies are lowest among all EOS as illustrated in Figure 6(c). STOS and HS(TM1) are followed by SFHx and SHFo (almost indistinguishable), while LS(220) results to highest average energies. This result is in agreement with the PNS contraction behaviors and hence growth timescale of the layer thickness of accumulated material above the PNS surface. The same ordering holds for $\bar{\nu}_e$ (see Figure 6(c)) due to the same phenomenon since they decouple at only slightly higher densities and hence equally thermalize from inelastic scattering on electrons/positrons crossing the layer of accumulated material above the PNS before reaching the free-streaming regime. $\nu_{\mu/\tau}$ and $\bar{\nu}_{\mu/\tau}$ decouple at higher densities, ($\sim 10^{13} \text{ g cm}^{-3}$) due to the absence of charged-current contributions. They can be used to directly probe the PNS contraction behavior, as illustrated in Figures 4 and 5, which is sensitive to intermediate-density EOS differences. This is also true for electron-favor neutrinos: the least(most) compact configuration STOS(220) results in lowest(highest) average ($\nu_{\mu/\tau}$, $\bar{\nu}_{\mu/\tau}$) energies. For additional insights regarding the evolution of neutrino luminosities and average energies comparing different nuclear EOS, see Hempel et al. (2012). The generally low average energies found here for the stiff STOS and HS(TM1) EOSs disfavor the neutrino-heating mechanism for shock revival. This has been probed in multi-dimensional SN simulations by and Suwa et al. (2013) comparing STOS and LS EOSs, and in an earlier work by Marek et al. (2009) for different EOS. Note that Swesty et al. (1994) found that different symmetry energies gave rise to markedly different evolutions of the electron neutrino luminosities, but a detailed comparison is difficult because some processes, like bremsstrahlung, were not included previously.

In addition to the simulations using the $11.2 M_{\odot}$ progenitor from Woosley et al. (2002), we also include the more massive $40 M_{\odot}$ progenitor from Woosley & Weaver (1995) into our EOS comparison in SN simulations. This progenitor has been discussed before within the scenario of black hole formation, also explored for the LS and STOS SN EOSs (see, e.g., Sumiyoshi et al. 2006, 2007; Nakazato et al. 2008, 2010b; Fischer et al. 2009; O'Connor & Ott 2011; Hempel et al. 2012). The moment of black hole formation is defined, within our general relativistic framework (for details, see Liebendoerfer et al. 2004), as the central lapse function approaches zero and stable numerical solutions for the evolution equations

**Figure 7.** Central density evolution for the $40 M_{\odot}$ model, comparing the EOSs under investigation.

(A color version of this figure is available in the online journal.)

cannot be obtained anymore. The lapse function determines time dilatations and gravitational Doppler shift effects. Note that core-collapse events which result in a black hole instead of an explosion are as bright as normal SN explosions with respect to the neutrino signal. The possible future detection of such a neutrino signal from a Galactic event may be used to further constrain the high-density EOS; see Nakazato et al. (2010a).

The moment of black hole formation, see t_{pb} in Table 5, is approached during the post-bounce evolution, during which the mass enclosed inside the PNS grows continuously in the absence of an explosion. The timescale for the central density (and also temperature) rise is given by the PNS contraction behavior, which in turn depends on the nuclear EOS. We list selected properties at the onset of PNS collapse in Table 5 for all EOS under investigation, ordered according to t_{pb} with the fastest (LS(180)) at the top and slowest (STOS) at the bottom. The PNS compression can be illustrated best via the central density evolution, shown in Figure 7. The values of the central density cluster around only two different values, 3.2×10^{14} and $2.5 \times 10^{14} \text{ g cm}^{-3}$, immediately after the bounce. It is likely that this is related to the properties of the EOS at low density, and thus also to the radii of very low mass neutron stars. A similar (but not exact) clustering is observed in the lower right-hand corner of Figure 2 where STOS, HS(TM1), and HS(FSUGold) have larger radii for $0.4 M_{\odot}$ neutron stars. This grouping lasts only for 300 ms after which time the EOS at higher densities becomes important.

HS(TMA) has a higher incompressibility but lower symmetry energy than STOS (which uses TM1) and leads to a significantly shorter (about 300 ms) accretion time until black hole formation (see Figure 7). This would indicate that the symmetry energy plays the dominant role. However, SFHo and SFHx do not obey this trend. Even though SFHo has a higher incompressibility and higher symmetry energy than SFHx, it leads to a shorter (about 50 ms) accretion time until black hole formation. Instead of using nuclear matter properties, one would expect that our results can be explained by the maximum mass of cold neutron stars, which is an integrated quantity of the EOS. However, by comparing the times until black hole formation (from Table 5) with the numbers in Table 2, it turns out that there is no

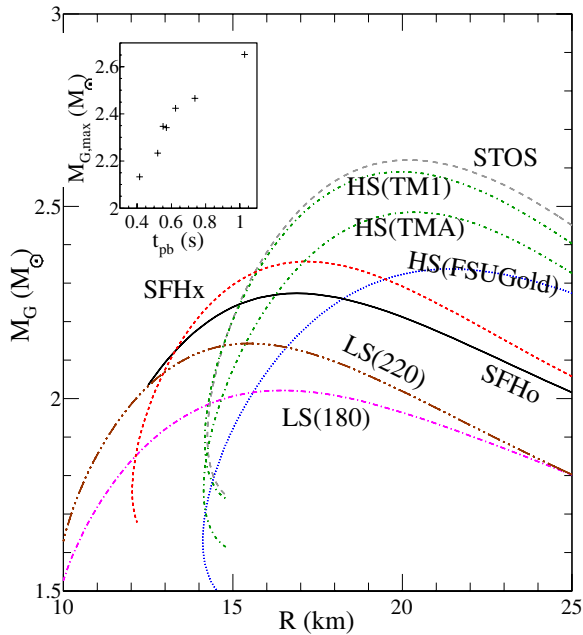


Figure 8. Mass–radius relations at constant entropy per baryon of $4 k_B$ comparing the EOSs under investigation. (A color version of this figure is available in the online journal.)

monotonic correlation. For example, the collapse of FSUgold occurs about 160 ms later than for LS(180), even though the maximum mass of LS(180) is $0.1 M_\odot$ larger.

Note that the two RMF EOS parameterizations, TM1 and TMA, fail to fulfill both zero temperature maximum mass and radius constraints, while LS(220) is on the edge of current acceptance; see Figure 2. The RMF EOSs based on TM1 and TMA result in sufficiently high maximum masses but give at the same time radii which are too large. With the black hole formation scenario explored here, these large radii are due to slower PNS contractions which results in an extended post-bounce mass accretion period until black hole formation (see Figure 7). On the other hand, FSUgold results in reasonably small neutron star radii but fails to fulfill the current maximum zero temperature mass constrain of $1.97 \pm 0.04 M_\odot$. It leads to a significantly shorter time until black hole formation than for TMA and TM1, however, comparable to SFHo. The latter has a larger incompressibility but slightly lower symmetry energy than FSUgold. On the other hand, SFHo and SFHx both fulfill mass and radius constraints by construction. It is interesting that the models which fulfill the mass–radius and maximum mass constraints, i.e., LS(220), SFHo, and SFHx, give rather similar values for t_{pb} , which seems to be constrained to 500–650 ms. It indicates that neutron star radius measurements constrain the time to black hole formation for $40 M_\odot$ progenitors.

Hempel et al. (2012) demonstrated that maximum neutron star mass determined from the EOS in beta-equilibrium at $s = 4 k_B$ baryon $^{-1}$ was strongly correlated with the time until black hole formation. This time can be measured with currently available neutrino detectors given a galactic core-collapse SN. The associated mass versus radius curves and their relationship with the time to black hole formation is displayed in Figure 8 for the EOSs under investigation. The corresponding values are also listed in the last column of Table 2. Note that the maximum masses increase for all EOS compared to the $T = 0$ case (compare also Figures 8 and 2). Pressure is more sensitive than energy density to the temperature effects because of the large nucleon mass and thus larger temperatures increase the

maximum mass. If we compare the maximum masses of the $s = 4 k_B$ baryon $^{-1}$ configurations from Table 2 with the time until black hole formation from Table 5, we find that these quantities have the same ordering, i.e., show an (almost) strictly monotonic correlation, which is also visible in the inset of Figure 8.

The correlation suggests the idea to extract information about the specific heat for a further explanation of the interesting temperature effects. The nucleon specific heat capacity is related to the nucleon effective mass m^* . In LS(220) the nucleon effective mass is always equal to the vacuum mass, whereas in the RMF models one typically has $m^*/m \sim 0.7$ at saturation density. For LS, the increase of the maximum mass $\Delta M_{\text{Max}} = M_{s=4, \text{Max}} - M_{T=0, \text{Max}}$ from $T = 0$ to $s = 4 k_B$ baryon $^{-1}$ is the lowest of the models investigated here (see Table 2). This is consistent with the high value of m^* in LS, as noted by Hempel et al. (2012) before. Looking also at the numbers of the other EOS in Table 2, there seems to be a correlation between ΔM_{Max} and m^*/m . However, we found that this correlation is clearly broken for other EOS not used here, e.g., DD2 from Typel et al. (2010). There are several other effects which play a role. The symmetry energy determines the electron fraction and thus changes the total specific heat. Furthermore, the $T = 0$ and symmetric EOS has an impact on the relevant densities which are actually reached in the PNS. Work on analyzing the finite-temperature behavior of these EOSs is in progress.

4. SUMMARY AND CONCLUSIONS

Recent neutron star radii measurements from observations of low-mass X-ray binary systems from Steiner et al. (2010) indicate small neutron star radii of about 11.5 km for canonical neutron stars of around $1.4 M_\odot$. It is also consistent with recent developments in chiral perturbation theory and quantum Monte Carlo (see Hebeler & Schwenk 2010; Steiner & Gandolfi 2012). In addition, neutron stars can be as massive as $1.97 \pm 0.04 M_\odot$ (see Demorest et al. 2010). Note that the most commonly used RMF EOS used in SN studies violate either one, if not all, of the aforementioned constraints. Motivated from these insights, we developed two new RMF interactions from which we constructed the two new SN EOSs, SFHo and SFHx, in such a way to fulfill all observational constraints. Moreover, the new EOSs are consistent with nuclear experimental constraints on matter near and below the saturation density. These new EOSs provide more variation in the set of EOS tables which can be used by the core-collapse SN community instead of commonly used EOSs based on, e.g., TM1 which is now ruled out by observations.

The new EOS were implemented in core-collapse SN simulations of massive iron-core progenitors. We compared the results with the commonly used non-relativistic EOS of Lattimer & Swesty (1991) and the RMF EOS of Shen et al. (1998). Moreover, we include into our EOS comparison also the recently introduced RMF EOS from Hempel & Schaffner-Bielich (2010) based on the parameterizations TM1, TMA, and FSUgold. We compared the different EOS during the iron-core collapse phase, which is dominated by heavy nuclei, and confirmed already reported differences between these EOS (see, e.g., Hempel et al. 2012). We extend the analysis and include SFHo/SFHx. Differences become large only slightly before and after core bounce, when the central density exceeds normal nuclear matter density. The post-bounce mass accretion phase prior to the possible onset of an explosion is ideal to study the PNS contraction behavior,

which reflects the EOS underlying nuclear matter properties for a given progenitor choice. In general, it is difficult to disentangle the relationship between individual nuclear matter properties, given at zero temperature near the saturation density, and the outcome of our SN simulations. This is related to the presence of correlations among the nuclear matter properties from nuclear systematics, which do not allow to vary them independently (see, e.g., Swesty et al. 1994). Nevertheless, we find that higher symmetry energies typically lead to higher Y_e , but only for EOS models which use the same description of nuclei at subsaturation densities. In a similar way, the central density obtained at bounce can be related to the value of the density derivative of the symmetry energy, L , if differences in the compressibility, K , are not too large. Also for the evolution of the shock radius and the neutrinosphere radius, we observe some impact of L , but also see a weak dependence on the other nuclear matter parameters and on the model description of nuclei at subsaturation densities. We find that the evolution of the average neutrino energies reflects the PNS contraction behavior and has a stronger imprint of the EOS than the evolution of neutrino luminosities. We also find a trend that the EOSs with large(low) symmetry energies result in low(high) average neutrino energies as a direct consequence of the slow(fast) PNS contraction behaviors. This may have consequences for shock revival via neutrino heating in multi-dimensional core-collapse SN simulations, where low neutrino energies result in less optimistic conditions since the heating rates scale with the neutrino energy squared. From this analysis, it may allow us to rule out some of the extreme EOS from the observation of a future galactic event.

We also find the EOS classifications “soft” or “stiff” misleading. Implicitly what is meant by soft or stiff is that the EOS has a lower or higher pressure. However, core-collapse SNe explore a large range of densities and temperatures, and an EOS which has a higher pressure at one density and temperature may have a lower pressure at another density and temperature. This is particularly evident with the black hole formation time as described here and in Hempel et al. (2012). EOSs like SFHx which have a low pressure at zero temperature near the saturation density have a longer time until black hole formation than the other EOSs because their pressure at $s = 4$ is larger. The addition of quark degrees of freedom at supersaturation density only further complicates this issue (see, e.g., Nakazato et al. 2008, 2010a, 2010b; Fischer et al. 2011). Note that the possible appearance of quark matter in SN explosions is still under debate.

Moreover, we explored the possible correlation between the EOS and outcome of the black hole formation scenario in the absence of an SN explosion. We confirm the analysis of Hempel et al. (2012), where only a correlation between finite entropy per baryon configurations of static PNSs and the time until black hole formation was found. Note that the neutrino signals of these events are as bright as ordinary SN explosions. But at the moment of black hole formation the signal suddenly stops which makes this time measurable with neutrino telescopes. The possible future neutrino observation of such a Galactic event will constrain the high-density and finite-entropy EOS significantly, complementary to future neutron star mass and radius observations.

This study implied that it is difficult to understand the effect of the EOS in core-collapse SNe by analyzing non-exploding models. To tackle the impact of the EOS on the explosion mechanism, multi-dimensional simulations are necessary (see, e.g., Marek et al. 2009; Couch 2013; Suwa et al. 2013). Furthermore, it remains to be explored how different nuclear

EOS can influence long-term cooling of (proto)neutron stars after the SN explosion has been launched. Therefore, the implementation of weak processes consistent with the nuclear EOS is required (see, e.g., Reddy et al. 1998, 1999). This may impact the neutrino cooling timescale and also the extent of PNS convection as studies recently described by Roberts et al. (2012b). The nuclear EOS may also be important for the proton-to-baryon ratio of the material ejected from the PNS surface known as neutrino-driven wind relevant for the nucleosynthesis of heavy elements. Moreover, a possible EOS impact within the cooling of PNSs on the emitted neutrino signal may also be of relevance for neutrino oscillation studies, in particular those which explore collective phenomena in the presence of large neutrino but small matter densities.

The authors thank S. Reddy, L. Roberts, and I. Sagert for several discussions on this work. The supernova simulations were performed at the computer center of the Helmholtzzentrum für Schwerionenforschung GmbH (GSI) in Darmstadt, Germany. A.W.S. was supported by DOE grant DE-FG02-00ER41132. M.H. and T.F. are grateful for support from CompStar, a research networking program of the ESF. M.H. acknowledges support from the High Performance and High Productivity Computing (HP2C) project, the Swiss National Science Foundation (SNF) under project number No. 200020-132816/1, and ENSAR/THEXO. T.F. is supported by the Swiss National Science Foundation under project No. PBBSP2-133378 and by the Narodowe Centrum Nauki (NCN) within the “Maestro” program under contract No. DEC-2011/02/A/ST2/00306.

REFERENCES

- Agrawal, B. K., Sulaksono, A., & Reinhard, P.-G. 2012, *NuPhA*, **882**, 1
- Audi, G., Wapstra, A. H., & Thibault, C. 2003, *NuPhA*, **729**, 337
- Baron, E., Cooperstein, J., & Kahana, S. 1985, *PhRvL*, **55**, 126
- Bethe, H. A., & Wilson, J. R. 1985, *ApJ*, **295**, 14
- Bruenn, S. W. 1985, *ApJS*, **58**, 771
- Buras, R., Janka, H.-T., Keil, M. T., Raffelt, G. G., & Rampp, M. 2003, *ApJ*, **587**, 320
- Burrows, A., Livne, E., Dessart, L., Ott, C., & Murphy, J. 2006, *ApJ*, **640**, 878
- Colo, G., Van Giai, N., Meyer, J., Bennaceur, K., & Bonche, P. 2004, *PhRvC*, **70**, 024307
- Couch, S. M. 2013, *ApJ*, **765**, 29
- Demorest, P. B., Pennucci, T., Ransom, S. M., Roberts, M. S. E., & Hessels, J. W. T. 2010, *Natur*, **467**, 1081
- Fatoyev, F. J., Horowitz, C. J., Piekarewicz, J., & Shen, G. 2010, *PhRvC*, **82**, 055803
- Fischer, T., Sagert, I., Pagliara, G., et al. 2011, *ApJS*, **194**, 39
- Fischer, T., Whitehouse, S. C., Mezzacappa, A., Thielemann, F.-K., & Liebendörfer, M. 2009, *A&A*, **499**, 1
- Fischer, T., Whitehouse, S., Mezzacappa, A., Thielemann, F.-K., & Liebendörfer, M. 2010, *A&A*, **517**, A80
- Hannestad, S., & Raffelt, G. 1998, *ApJ*, **507**, 339
- Hebeler, K., Lattimer, J. M., Pethick, C. J., & Schwenk, A. 2010, *PhRvL*, **105**, 161102
- Hebeler, K., & Schwenk, A. 2010, *PhRvC*, **82**, 014314
- Hempel, M., Fischer, T., Schaffner-Bielich, J., & Liebendörfer, M. 2012, *ApJ*, **748**, 70
- Hempel, M., & Schaffner-Bielich, J. 2010, *NuPhA*, **837**, 210
- Hempel, M., Schaffner-Bielich, J., Typel, S., & Röpke, G. 2011, *PhRvC*, **84**, 055804
- Horowitz, C. 2002, *PhRv*, **D65**, 043001
- Juodagalvis, A., Langanke, K., Hix, W. R., Martínez-Pinedo, G., & Sampaio, J. M. 2010, *NuPhA*, **848**, 454
- Khan, E., & Margueron, J. 2012, *PhRvL*, **109**, 092501
- Lalazissis, G. A., König, J., & Ring, P. 1997, *PhRvC*, **55**, 540
- Lattimer, J. M., & Lim, Y. 2013, *ApJ*, **771**, 51
- Lattimer, J. M., & Swesty, F. 1991, *NuPhA*, **535**, 331
- LeBlanc, J., & Wilson, J. 1970, *ApJ*, **161**, 541

- Liebendoerfer, M., Messer, O., Mezzacappa, A., et al. 2004, [ApJS](#), **150**, 263
- Marek, A., Janka, H.-T., & Müller, E. 2009, [A&A](#), **496**, 475
- Martínez-Pinedo, G., Fischer, T., Lohs, A., & Huther, L. 2012, [PhRvL](#), **109**, 251104
- Mezzacappa, A., & Bruenn, S. 1993a, [ApJ](#), **410**, 740
- Mezzacappa, A., & Bruenn, S. 1993b, [ApJ](#), **405**, 637
- Mezzacappa, A., & Messer, O. E. B. 1999, [JCoAM](#), **109**, 281
- Mohr, P. J., Taylor, B. N., & Newell, D. B. 2008, [RvMP](#), **80**, 633
- Möller, P., Nix, J. R., Myers, W. D., & Swiatecki, W. J. 1995, [ADNDT](#), **59**, 185
- Nakazato, K., Sumiyoshi, K., Suzuki, H., & Yamada, S. 2010a, [PhRvD](#), **81**, 083009
- Nakazato, K., Sumiyoshi, K., & Yamada, S. 2008, [PhRvD](#), **77**, 103006
- Nakazato, K., Sumiyoshi, K., & Yamada, S. 2010b, [ApJ](#), **721**, 1284
- O'Connor, E., & Ott, C. D. 2011, [ApJ](#), **730**, 70
- Piekarewicz, J. 2010, [JPhG](#), **37**, 064038
- Qin, L., Hagel, K., Wada, R., et al. 2012, [PhRvL](#), **108**, 172701
- Reddy, S., Prakash, M., & Lattimer, J. M. 1998, [PhRvD](#), **58**, 013009
- Reddy, S., Prakash, M., Lattimer, J. M., & Pons, J. A. 1999, [PhRvC](#), **59**, 2888
- Roberts, L. F., Reddy, S., & Shen, G. 2012a, [PhRvC](#), **86**, 065803
- Roberts, L. F., Shen, G., Cirigliano, V., et al. 2012b, [PhRvL](#), **108**, 061103
- Shen, G., Horowitz, C. J., & O'Connor, E. 2011a, [PhRvC](#), **83**, 065808
- Shen, G., Horowitz, C. J., & Teige, S. 2011b, [PhRvC](#), **83**, 035802
- Shen, H., Toki, H., Oyamatsu, K., & Sumiyoshi, K. 1998, [NuPhA](#), **637**, 435
- Shlomo, S., Kolomietz, V. M., & Coló, G. 2006, [EPJA](#), **30**, 23
- Steiner, A. W., & Gandolfi, S. 2012, [PhRvL](#), **108**, 081102
- Steiner, A. W., Lattimer, J. M., & Brown, E. F. 2010, [ApJ](#), **722**, 33
- Steiner, A. W., Lattimer, J. M., & Brown, E. F. 2013, [ApJL](#), **765**, L5
- Steiner, A. W., Prakash, M., Lattimer, J. M., & Ellis, P. J. 2005, [PhR](#), **411**, 325
- Sugahara, Y., & Toki, H. 1994, [NuPhA](#), **579**, 557
- Suleimanov, V., Poutanen, J., Revnivtsev, M., & Werner, K. 2011, [ApJ](#), **742**, 122
- Sumiyoshi, K., Suzuki, H., & Toki, H. 1995, [A&A](#), **303**, 475
- Sumiyoshi, K., Yamada, S., & Suzuki, H. 2007, [ApJ](#), **667**, 382
- Sumiyoshi, K., Yamada, S., Suzuki, H., & Chiba, S. 2006, [PhRvL](#), **97**, 091101
- Suwa, Y., Takiwaki, T., Kotake, K., et al. 2013, [ApJ](#), **764**, 99
- Swesty, F. D., Lattimer, J. M., & Myra, E. S. 1994, [ApJ](#), **425**, 195
- Tews, I., Krueger, T., Hebeler, K., & Schwenk, A. 2013, [PhRvL](#), **110**, 032504
- Timmes, F. X., & Arnett, D. 1999, [ApJS](#), **125**, 277
- Todd-Rutel, B. G., & Piekarewicz, J. 2005, [PhRvL](#), **95**, 122501
- Toki, H., Hirata, D., Sugahara, Y., Sumiyoshi, K., & Tanihata, I. 1995, [NuPhA](#), **588**, 357
- Tsang, M. B., Stone, J. R., Camera, F., et al. 2012, [PhRvC](#), **86**, 015803
- Tsang, M. B., Zhang, Y., Danielewicz, P., et al. 2009, [PhRvL](#), **102**, 122701
- Typel, S., Röpke, G., Klähn, T., Blaschke, D., & Wolter, H. H. 2010, [PhRvC](#), **81**, 015803
- Woosley, S., Heger, A., & Weaver, T. 2002, [RvMP](#), **74**, 1015
- Woosley, S., & Weaver, T. 1995, [ApJS](#), **101**, 181